nature electronics

Article

https://doi.org/10.1038/s41928-023-01075-y

Clean assembly of van der Waals heterostructures using silicon nitride membranes

In the format provided by the authors and unedited

Contents:

1 SiN_x cantilever fabrication 2

Figure S1. Fabrication of SiN_x cantilevers. 2

2 Cantilever transfer: Heterostructure assembly in air and inert gases 3

Figure S2. Illustration for polymer-free heterostructure assembly. 4

Figure S3. Heterostructures with CVD-grown 2D materials. 5

Figure S4. Comparison of multilayer heterostructures fabricated using polymer and inorganic transfers. 6

3 Laminate transfer: Scalable heterostructure fabrication 7

Figure S5. Schematic of the scalable SiN_x membrane assisted transfer process. 7

4 UHV system design 10

4.1 Key components 10

Figure S6. Schematic overview of the UHV stacking system 11

4.2 UHV transfer setup 11

4.3 Loading samples 12

4.4 Optical setup 12

5 UHV sample annealing protocol 13

Table S1. Annealing procedure. 13

6 Polymer stamp transfer in UHV 14

Figure S7. Optical image sequence demonstrating the formation of a melt spot and subsequent flakes pickup in UHV using the polymer stamp method. 15

Figure S8. Sequence to fabricate hBN/graphene/hBN heterostructures in UHV using the polymer stamp method. 15

7 Atomic Force Microscopy 16

8 Cross-sectional STEM and EDX 17

Figure S9. Cross-sectional scanning transmission electron microscopy (STEM) energy dispersive X-ray spectroscopy (EDX) characterization. 17

Figure S10. Plan view scanning transmission electron microscopy (STEM) energy dispersive X-ray spectroscopy (EDX) characterization of metals deposited on the cantilever surface. 17

9 Mobilities Comparison 18

Table S2. Mobilities comparison (Drude Model). 18

Table S3. Mobilities comparison (MFP). 20

1 SiN_x cantilever fabrication

The cantilevers were fabricated by selectively etching double-sided 500 nm SiN_x coated Si wafers, illustrated in Fig.S1(a), purchased from Inseto UK. The nitride layers on both sides were then patterned using successive optical lithography and reactive ion etching (RIE) with SF_6 and CHF_3 mixed plasma. One side was patterned to act as a hard mask for the Si wet etch (b), while the other was patterned to define the cantilever geometry (c). The resist etch mask was removed using oxygen plasma, and the sample was immersed in KOH (aq. 30 %, 80 °C, ~7 hours) to release the cantilever and define the supporting Si chip by selectively etching away the exposed regions. After rinsing in solvents, the wafer-scale cantilever array can be separated into small pieces for subsequent metal coating and 2DMs transfers.

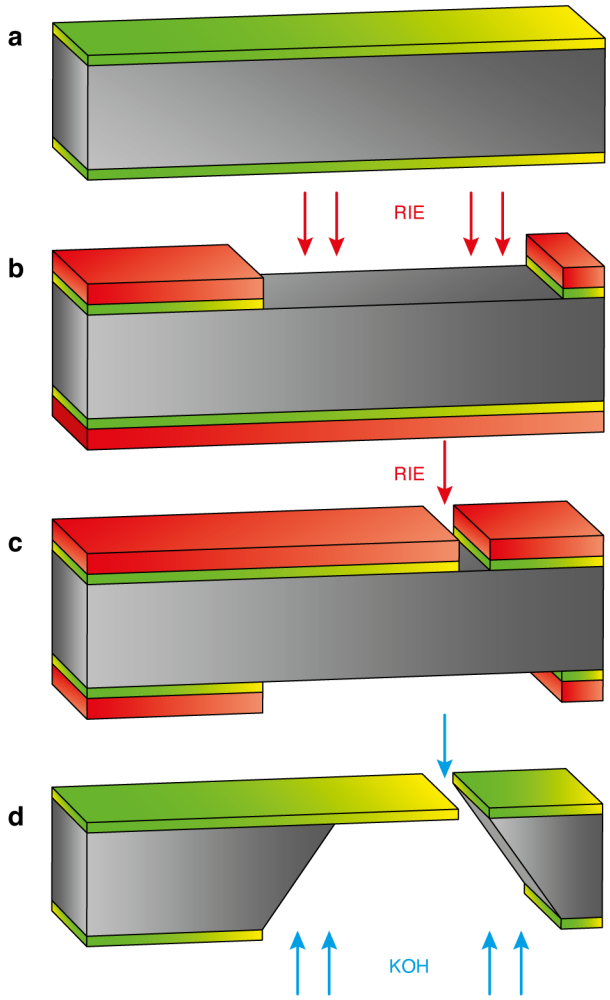

Figure S1. Fabrication of SiN_x cantilevers. *(**a**) Initial Si wafer coated with SiN_x on both sides. (**b**) Optical lithography and RIE used to define the wet etch hard mask on one side. (**c**) The sample is flipped, and the cantilevers are defined on the other side. (**d**) KOH solution is used to remove the silicon from the area defined by the etch mask in (b), releasing the SiN_x cantilever.*

2 Cantilever transfer: Heterostructure assembly in air and inert gases

The polymer-free transfer based on cantilevers utilizes the van der Waals adhesion force to assemble heterostructures without the use of any polymers in the process. To improve the adhesion of SiN_x, the cantilevers are coated with 1nm Ta, 5nm Pt, and 0.65nm Au. The key factor for achieving optimal adhesion is the Au thickness: for instance, for a 0.1 nm thick Au layer the pickup of 2D crystals becomes unreliable, while for 1nm thick Au the pick-up always works, but it becomes impossible to drop-off the assembled heterostructures from the cantilevers. Importantly, we also find that the adhesion of 2DM to the cantilevers decreases over time as a metal-coated surface is exposed to the air. For this reason, we perform the first 2DM pick-up within 20-30 minutes after the metal coating. This is most likely caused by the surface contamination progressively coating the gold layer and producing a noticeable change in adhesion, which becomes pronounced after ~1 hour of air contact. However, a quick plasma cleaning (several seconds) is sufficient to refresh the surface and allows re-use of old cantilevers.

To make an hBN-graphene-hBN stack, a freshly metal-coated cantilever is attached to the micromanipulator and aligned over a selected hBN crystal exfoliated on top of a 300 nm SiO_2/Si wafer. The cantilever is brought into contact with the surface which is heated to 120-150 °C for a few seconds, before the hBN crystal is carefully lifted off the oxide surface, (See Fig. S2(a-c)). Then, the hBN on the cantilever is aligned over a chosen graphene crystal (Fig.2(d)) (exfoliated from graphite supplied by graphit.de) on another 300 nm SiO_2/Si substrate. Both flakes are brought into contact and lifted away together with the substrate heated at 120°C. The whole process takes several seconds, which is much faster than polymer assisted methods (See Fig.S2(e-f)). We found that the best temperatures for monolayer graphene pick up are between 100-120 °C. If the temperature is higher than 150°C, the graphene may display cracks after the transfer (See Extended data Fig.1b). Lastly, the hBN-graphene stack on the cantilever can be dropped onto the bottom hBN (or graphite for other material combinations) at a temperature of 230°C or higher (see Fig.2(g-i)). We observed that even if bubbles have formed within the heterostructure layers on the previous stages of the process (when performing in air or glovebox environment), performing this last stage at a substantially higher temperature helps remove them from the stack, while not causing any fracturing in the already assembled layers.

We have also assembled heterostructures from 2D crystals exfoliated on spin-coated PMMA surfaces (Extended data Fig.1d,e). This polymer allows for exfoliation of much larger TMD crystals compared to conventional oxidized silicon, and is frequently used in the field for this reason. If lithography-grade PMMA is used, following the above methods yields similar results with >20µm large clean areas.

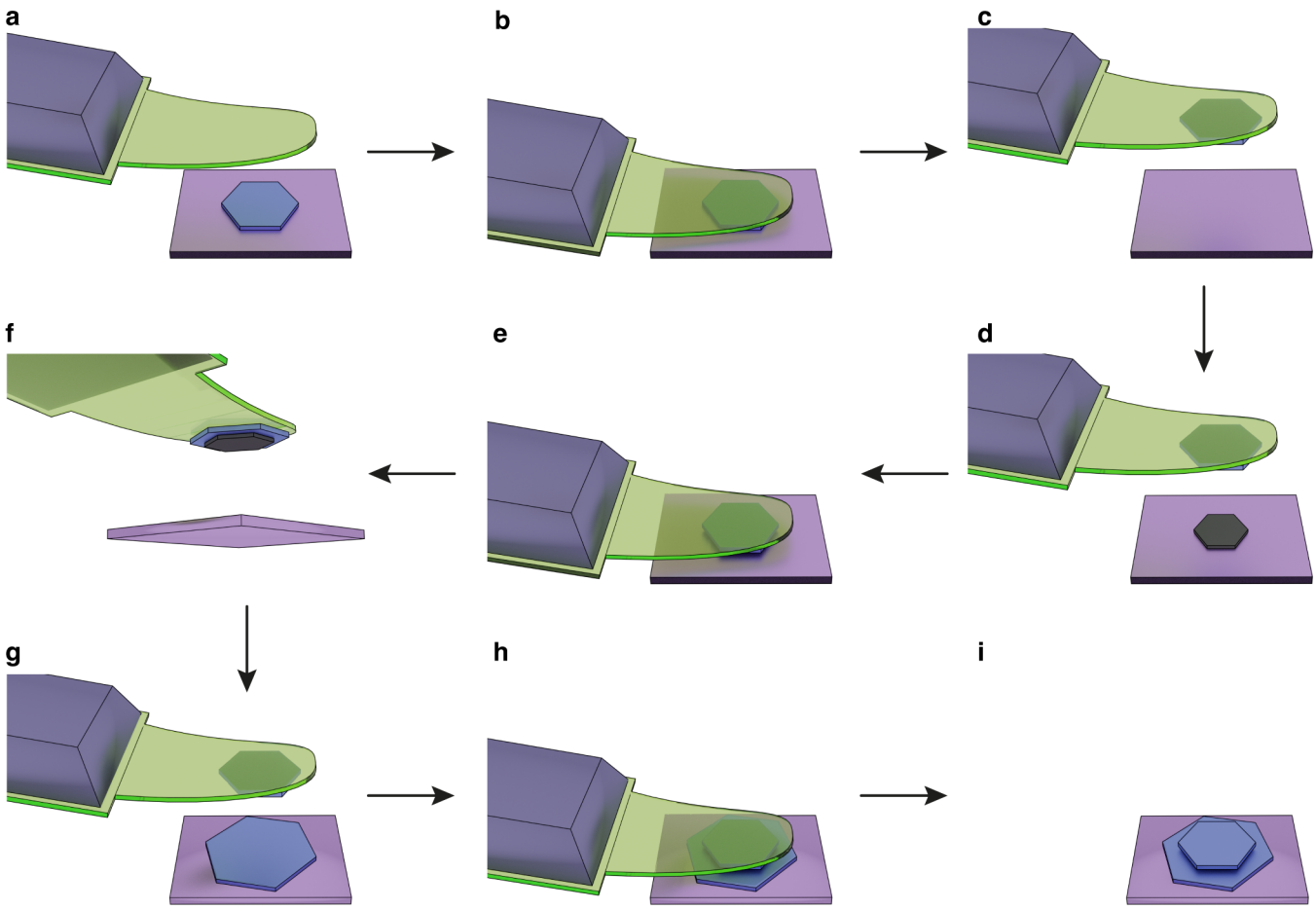

Figure S2. Illustration for polymer-free heterostructure assembly. *(**a**) Cantilever aligned above hBN crystal (hBN shown as blue hexagon). (**b**) Cantilever lowered to make contact with hBN. (**c**) Top hBN picked up by cantilever at 120 °C. (**d**) Top hBN aligned above a chosen graphene flake (graphene shown as black hexagon). (**e**) Cantilever lowered so top hBN contacted to graphene at 120 °C. (**f**) Graphene picked up by hBN. (**g**) hBN/graphene aligned above bottom hBN. (**h**) Cantilever lowered so top hBN and graphene and contacted to bottom hBN. (**i**) BN/graphene/hBN stack detached from cantilever and finished stack left on silicon oxide substrate.*

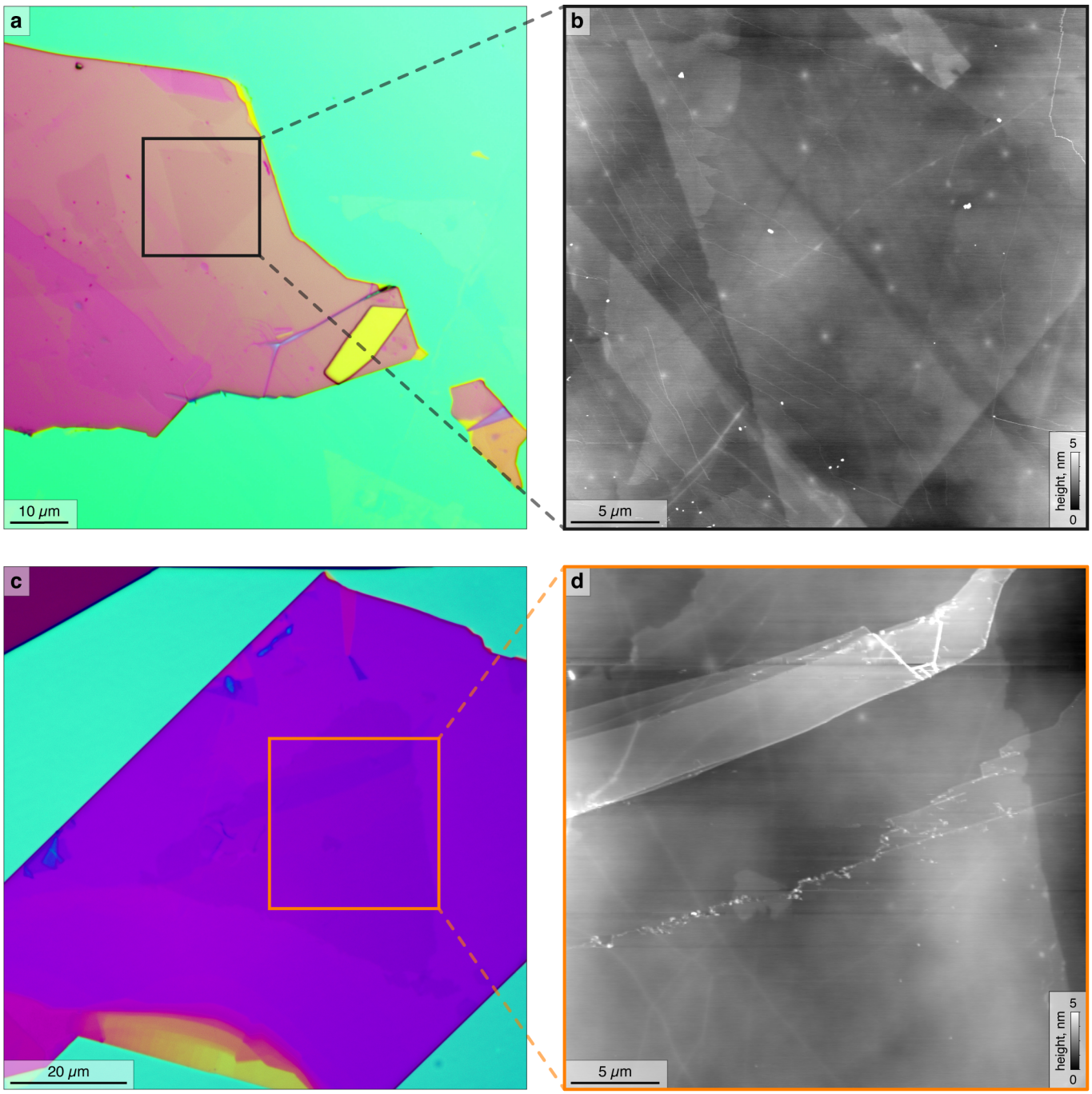

Figure S3. Heterostructures with CVD-grown 2D materials. *(**a,c**) Optical micrographs of CVD grown WS_2 monolayers picked up from their growth substrate (SiO_2) and encapsulated in hBN. Optical contrast is digitally enhanced to improve visibility (**b,d**) AFM topography maps of the indicated regions, featuring absence of the hydrocarbon pockets. The WS_2 was picked up at 150°C, and dropped off at 170°C.*

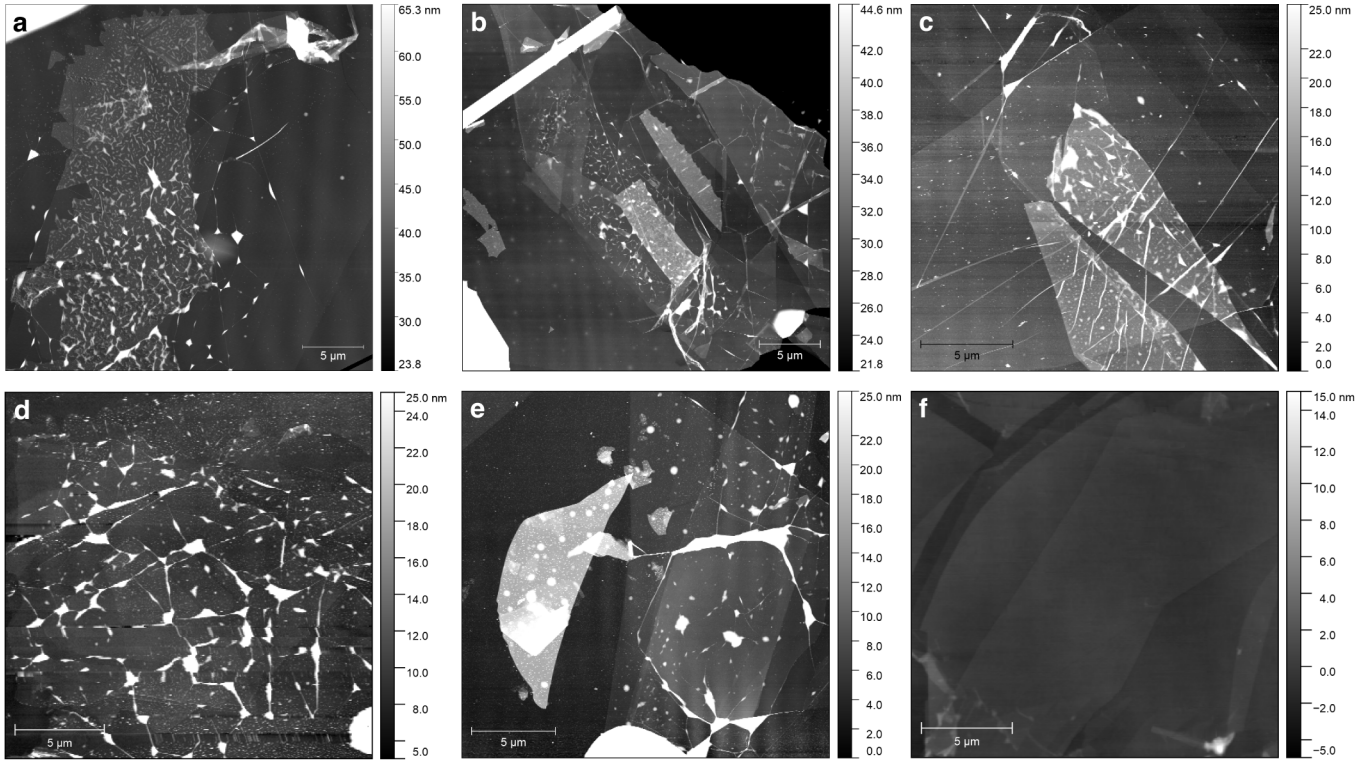

Figure S4. Comparison of multilayer heterostructures fabricated using polymer and inorganic transfers. *Large area AFM Topography images of LED devices formed from 6 individual 2D crystals, with (a-c) 5L, 7L, and 4L InSe respectively, and (d-f) monolayer WS_2, WSe_2, and WS_2 respectively. Stacks were fabricated using state of the art polymer transfer techniques (a-e) and our inorganic method (f) in an argon glovebox environment. No bubbles or wrinkles are visible in the stack fabricated using the inorganic technique despite the 6 interfaces. In all cases the optically active layer is sandwiched with thin 2-4 layer hBN, followed by graphene electrodes, and finally capped with a thick hBN encapsulation layer.*

3 Laminate transfer: Scalable heterostructure fabrication

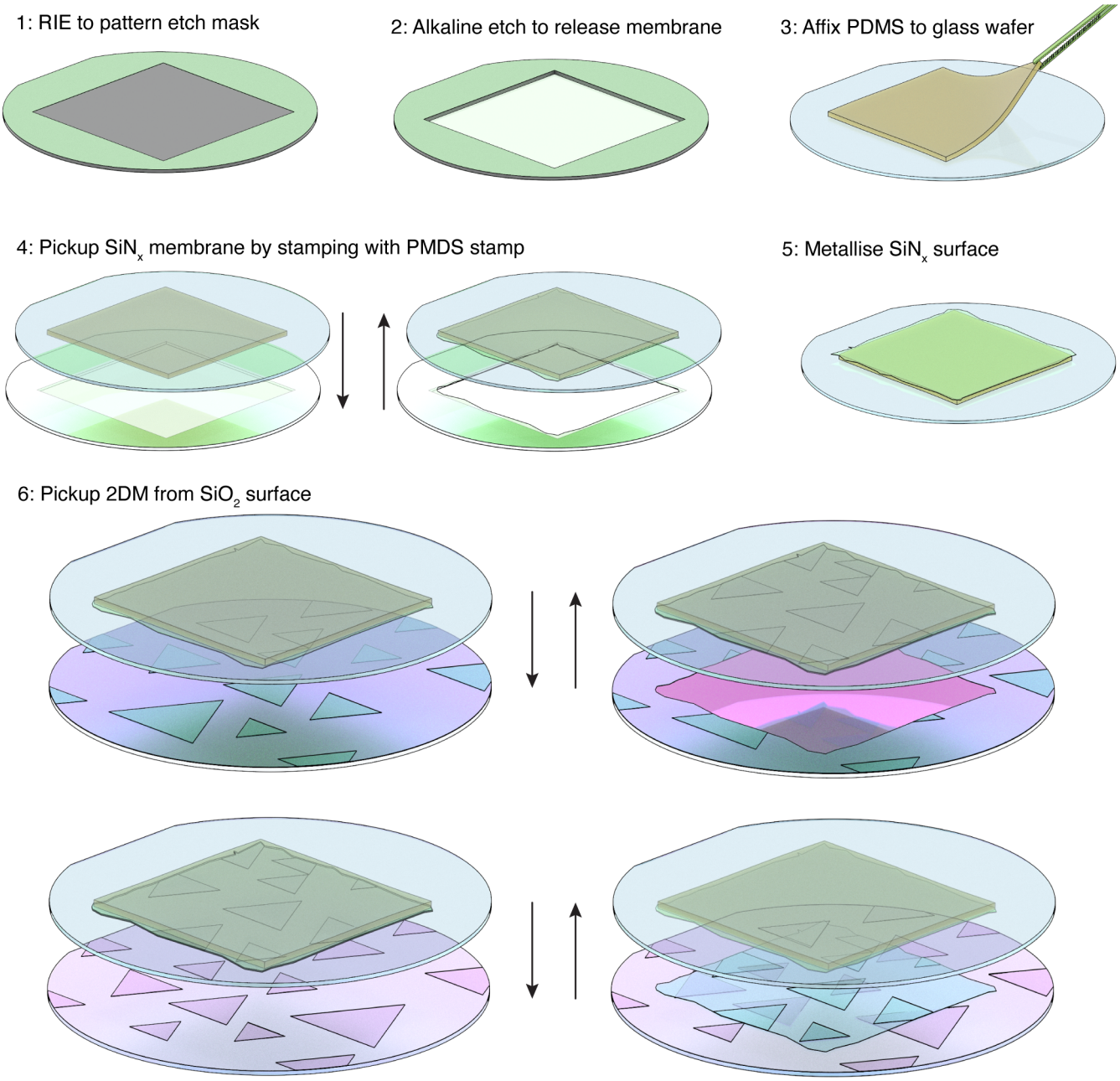

Figure S5. Schematic of the scalable SiN_x membrane assisted transfer process. *Individual steps are described in the main text.*

The scalable transfer process is schematically illustrated in Supplementary Figure S5. The sequence of steps required to fabricate the PDMS/ SiN_x/ metal laminate, and then use it to transfer a CVD grown TMD are listed below.

1. Double side polished and SiN_x coated wafers are purchased from Inseto UK. Rectangles aligned parallel to the Si crystalline direction are opened in the SiN_x layer on one side of the wafer to act as an etch mask for Si etching, using photolithography and subsequent reactive ion etching (SF_6 + CHF_3).
2. The wafer is then etched (KOH 30% w/v aq. @ 60°C) to remove the Si where the SiN_x was removed, leaving freestanding SiN_x membranes on the opposite side of the wafer.
3. PDMS film (1mm thickness Gel Pak type 4) is cut to the required size and carefully placed on a clean transparent substrate.
4. The PDMS film is brought into contact with the SiN_x membrane while the membrane temperature is held at 150°C. The area of the PDMS stamp should be entirely within the area of freestanding SiN_x membrane. The transparent substrate is then carefully lifted away, raising the PDMS stamp, causing the freestanding area of SiN_x membrane to fracture around the edge of the stamp.
5. The PDMS supported SiN_x surface is metallised by depositing the specified metallic adhesion layers.
6. The stamp can then be used to perform stamping assembly of vDW heterostructures. In the example shown in Supplementary figure S5, the stamp is first brought into contact with a large area TMD film grown on silicon oxide. If the substrate is heated to 150C, raising the stamp after a few seconds of contact delaminates the CVD from the oxide. The carried material can then be deposited on a TMD film CVD grown on sapphire – the greater adhesion of the lower TMD to the substrate in this case means that the stack remains on the substrate and is delaminated from the metal film on the SiN_x stamp.

The stamping technique developed here is based on a balance of adhesive forces – for pickup to be successful the adhesion of the material to the metallized SiN_x must exceed that to its original substrate. But as the adhesive forces are critically dependent on the contact area, they are significantly influenced by relative surface roughness. All attempts to transfer mechanically exfoliated flakes in air and in an inert argon environment were successful,and resulted in bubble- and contamination-free heterostructures, although it is a slightly more laborious process than using the cantilever geometry. However, the flatness requirement limited the range of CVD grown materials which could be successfully transferred – by their nature they are fully conformal to their growth substrate, therefore any significant roughness in the growth substrate would prevent full contact with the transfer stack. Therefore, our attempts to pick up from metallic growth substrates were unsuccessful due to the significant surface roughness of the commercially supplied Cu foils. Pickup of materials grown directly onto Silicon oxide was only partially successful – limited in this case by the roughness of the 2D materials themselves (atomic steps and high “nucleation” points), as well as the technical difficulties of achieving planar alignment between the SiN_x surface and underlying material over cm-length scales.

Nevertheless, we were able to transfer an area corresponding to the scale of the thickness variations of the growth material. A region of thicker WS_2 is shown in the central area of Extended data Fig. 3b – lines were mechanically scratched into the WS_2 to enable visualization. Missing regions and thicker areas are clearly visible in the as-grown CVD material – however this region was about as large and relatively continuous area as we were able to grow or procure. The majority of the top monolayer is then shown after transfer to a second WS_2 material on a SiO_2 substrate in (b). On the right-hand side of the image, the presence of thicker layers of WS_2 on the growth substrate (which are more visible after transfer) have prevented local conformal contact, limiting the area of the transferred monolayer. In addition, dust particles caused by the mechanical scratching necessary to enable visualization of the layers during transfer have also resulted in small local holes in the transferred monolayer. However, AFM analysis and PL mapping (see Fig. 4 in main text) have demonstrated a high-quality interface, with the complete absence of bubbles or trapped contamination at the 2D heterostructure interface, as well as no wrinkles or cracks. The individual areas between the scratched lines and defects already represent the largest 'clean' heterostructure fabricated from CVD grown materials [L. Banszerus et al., *Nano Lett.* **16**, 2, p1387 (2016)], and the first not limited by the size of a mechanically exfoliated flake.

Furthermore, we are confident that the aforementioned technical problems can be addressed, and that our proof on concept demonstrates a viable system for large scale homogenous transfers. Whilst we were unable to grow or commercially source large-scale flat and homogenous 2D materials, recent developments such as growth of quasi suspended flat graphene directly on SiO_2 [H. Ci et al., *Adv. Mat.* **34,** 51, p2206389 (2022)], low temperature growth on ultraflat metallic foils [F. Pizzocchero., *ACS Omega* **7**, 26 p22626 (2022], and growth of uniform multilayer hBN [S. Fukamachi et al., *Nat. Electron.* **6**, p126 (2023)] would seem ideal candidates for direct stamping transfer. Indeed, we believe that large scale fabrication of the flat and homogenous 2DM structures as demonstrated here is impossible without such ultraflat growth substrates – it is simply impossible to transfer a 2DM conforming to a rough substrate to a flat configuration (such as in a heterostructure) without generating wrinkles or local strain variations.

4 UHV system design

4.1 Key components

Our Ultra-High Vacuum (UHV) system comprises a multi-chamber arrangement of several distinct stations connected by a transfer tunnel (TT) which is used to shuttle samples between different chambers using a magnetically manipulated cassette on rails. The operation of motors and the movement of samples between different stations along the TT is controlled by a human-machine interface (HMI) screen. In addition to the stacking and characterization system stations detailed below (Fig. S6), the system contains a deposition chamber for electron-beam/sputter deposition of metals.

The primary chamber used for assembly and optical characterization of heterostructures is referred to as the core chamber (CC). The CC is a large rectangular UHV chamber mounted on vibration-isolated support with a base pressure in the low 10^{-10} mbar range, pumped by a combination of scroll, turbo and ion pumps assisted by a titanium sublimation pump (TSP) and a non-evaporable getter (NEG). To achieve the base pressure the UHV chamber is baked-out for at least 48 hours at 140°C. A full exploded schematic showcasing the main components of the CC is shown in **Fig. S6**.

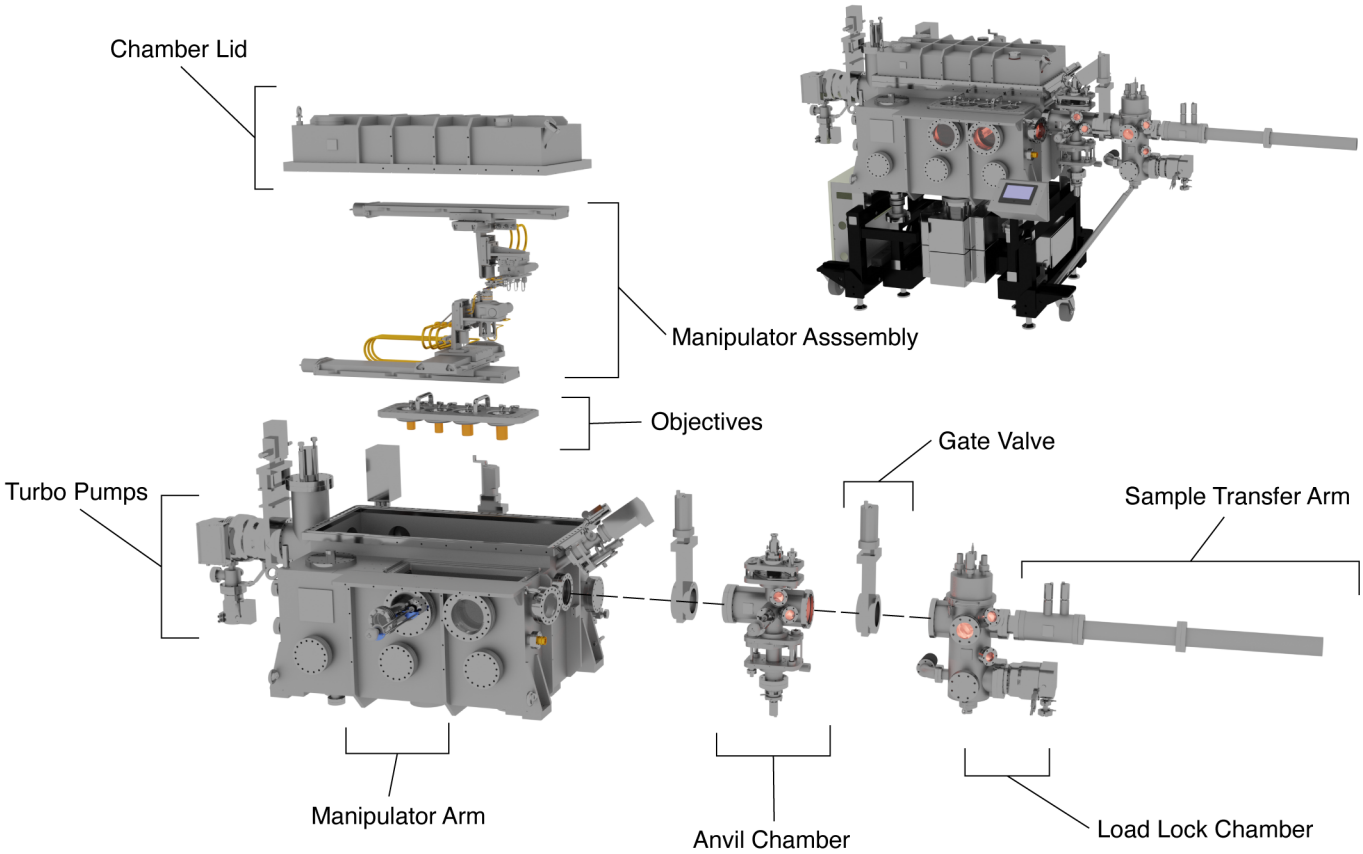

Figure S6. Schematic overview of the UHV stacking system highlighting the position of the main components comprising the core chamber (CC) and the load lock (LL). *Inside the CC, a set of optical objectives (5x, 20x, 50x, 100x) are mounted in fixed positions and enclosed by water-cooled copper jackets to avoid deformation and damage during the chamber bake-out processes. These objectives are employed to find and align the flakes, as in standard air/inert atmosphere transfers. A series of manipulators installed inside the CC facilitate the alignment and stacking of 2D heterostructures (discussed in section 1.3.2). Top right: Fully assembled CC system.*

4.2 UHV transfer setup

Within the UHV CC, there is manipulator assembly consisting of both a top and a bottom stage manipulator stacks (see **Fig.S6**) each consisting of high-precision (better than 1 µm) Physik Instrumentre (PI) XYZ manipulators. The bottom stage has an additional rotational stage (precision ± 0.01°) and the top stage assembly has both pitch and roll stages (precision ± 0.005°) to adjust the contact angle of the sample relative to the stamp/cantilever used to assemble the heterostructure. The stages are controlled using PI SMC Hydra controllers with movement instructions sent via ethernet using a custom-written LabView control program. This setup is also interfaced to a set of 2-axis hand controllers with variable precision for fine XYZ movement of the top and bottom stages independently, thereby allowing precise navigation within the CC.

The stages accept a common sample holder (Prevac PTS type) allowing a variety of sample sizes and processes to be performed on 2D material samples by moving the PTS holders around the system via the TT and the manually operated manipulators. The primary bottom stage used in this work has a 1-inch wafer holder, while the top stage takes a modified PTS with an extended plate design to allow mounting of microfabricated cantilevers/glass slides for pickup/deposition of 2D flakes for assembling stacks. The PTS holders connect via a ball-pen style locking mechanism mounted to a manually operated manipulator which can load a PTS holder to the top/bottom manipulator of the CC. PTS holders are held into the stages via a pneumatically driven coupling that mates the PTS to electrical contacts for heating and provides thermal contact for cooling using compressed gas flow. Both stages are capable of being resistively heated up to 1000°C.

4.3 Loading samples

Samples can be introduced into the main stacking chamber via two routes. For samples that require prior metal deposition, the transfer tunnel is used to deliver them from the deposition chamber into the CC without breaking vacuum. For samples loaded from the air, a HV load lock (LL) connected to the system allows the simultaneous loading of 3 PTS holders, as well as annealing and plasma cleaning prior to their introduction into the CC for stacking and optical characterization.

For flag-type transfers, a flag-type PTS is introduced to the system via the LL chamber, the flag is then extracted from the PTS using a manipulator arm in the CC (see **Fig. S6**) and slotted into the slip-stick stage manipulator.

4.4 Optical setup

To observe and guide the transfer process, we have designed a UHV-compatible optical microscope with the objectives fixed inside of the vacuum chamber while its other modules are placed in the air behind a quartz viewport. This arrangement provides high optical resolution, similar to that of a conventional optical microscope in air, while still allowing a full system bakeout at 150 °C after removing the air-side part of the optical assembly. Optical identification of 2D crystals and alignment of crystal stacks are performed by moving the top/bottom stages underneath the various magnitude objectives. The CMOS Nikon DS-Fi3 camera and illumination unit, both mounted outside of the system, are then moved by a stepper motor assembly to fixed positions directly above the desired objectives. Illumination is provided by a white LED light source via an epi-illuminator allowing for bright- and dark-field imaging.

5 UHV sample annealing protocol

To perform the 2D crystals assembly, graphene and hBN were first exfoliated using adhesive tape ex-situ from the UHV system in a class 100 cleanroom environment onto 300 nm SiO_2/Si wafers, and suitable graphene and hBN crystals were identified optically. When the 2D materials are brought into the UHV system, they must be annealed to remove adsorbed hydrocarbons and water vapor. The temperature, environment and time required to anneal materials varies and depends on the crystals intended use as well as the sample holder employed. Higher annealing temperatures will cause crystals to adhere more strongly to substrates so crystals that need to be delaminated from either the oxide substrates or cantilevers for “stamp transfers” must be annealed at lower temperatures. The cantilevers have a thin layer of e-beam deposited gold on the surface and thus, annealing them above 500°C causes restructuring of the Au layer, resulting in a very strong bond of the cantilever to the hBN or graphite and preventing delamination at later stages in the fabrication. Therefore, cantilevers are annealed below 450°C to allow the drop-off of the assembled 2D crystal stack. Nevertheless, this “permanent bonding” effect can be exploited for samples that will remain on the cantilever. The maximum operating temperature is also 2D material specific, high-temperature annealing can damage or alter the composition of some materials which can in turn, result in adverse effects on the performance. For example, graphene crystals annealed at 600°C were found to have reduced mobility values. For this reason, the UHV assembly in this work has been limited to graphene and boron nitride.

Samples on the bottom PTS holder to be picked up by the cantilever are annealed in the LL of the UHV system at 350°C overnight (>12h) at high vacuum (chamber pressure $5x10^{-7}$ mbar) and then for 15 minutes in a H_2/Ar atmosphere (gas mix pressure $5x10^{-2}$ mbar, ratio 1:10). For optimal results the bottom PTS is then loaded into the CC whilst still warm (150-100°C) to avoid hydrocarbon and water vapour condensing back on the sample before it is moved to the UHV environment and further annealed at 400°C for 1 hour in UHV (>10^{-9} mbar). The sample is then cooled to 150°C for the transfer. Between transfer steps the growing heterostructure is re-annealed on the cantilever at 350°C in UHV to remove any hydrocarbons and water vapor from underneath each crystal before the next layer is picked up.

Table S1. Annealing procedure.

Type	Step 1 – In LL HV	Step 2 – In LL H_2/Ar	Step 2 – In CC
Top PTS with cantilevers	350°C, overnight	350°C, 15 min	350°C, UHV, > 1 hour
Bottom PTS	350°C, overnight	350°C, 15 min	400°C, UHV, > 1 hour
Flag PTS	400°C, overnight	400°C, 10 min	400°C, UHV, > 1 hour

6 Polymer stamp transfer in UHV

For comparison, we have tested the performance of a conventional polymer transfer technique in UHV conditions. A disadvantage of this method is that regardless of how much they are annealed, polymers introduce mobile hydrocarbon contamination to the UHV system. A consequence of this is that despite the UHV environment, heterostructures stacks created using transfer polymers still suffer from contamination which can be observed as “bubbles” trapped between crystalline layers and visible in an optical microscopy image or by atomic force microscopy.

To perform polymer transfer in UHV conditions, 3% 950kDa PMMA is drop cast onto a glass slide (6mm x 25mm x 1 mm) and left to dry over several hours on a 30° downwards slope to create a high curvature meniscus. The stamp is then loaded into the UHV system, pumped in the LL ($>10^{-7}$ mbar) and annealed at 150°C for 6 hours to allow the PMMA to degas before being brought into the CC (see **Fig. S7a**). In order to pick up 2D flakes effectively, a flat spot is created on the surface of the PMMA. We do this by bringing the stamp into contact with a clean area of a target substrate at room temperature before increasing the temperature to ~ 100°C, which softens the PMMA and generates a flat region. After this, the stamp is rapidly retracted (**Fig. S7b**). The formation of a flat spot (> 100 x 100 µm) provides a repeatable first point-of-contact between the stamp and all future substrates which is useful for 2D crystal pickup and subsequent stacking operations. In addition, the “melt spot” allows precise control of the wetting front as the PMMA contacts the surface. Following the creation of the melt spot, the stamp can be used controllably to pick up flakes at ~ 70°C. A demonstration of this is provided in **Fig. S7c-e**.

To demonstrate the efficacy of the polymer stamp technique in UHV, several encapsulated hBN/Gr/hBN samples were fabricated. To achieve this, both graphene and hBN were exfoliated using adhesive tape ex-situ from the UHV system in a class 100 cleanroom environment onto 300 nm SiO_2/Si wafers. Then, suitable crystals were identified optically. The prepared wafers were then clamped onto heated PTS holders and annealed at 400°C in the high vacuum LL overnight before introduction to the CC for flake identification and stacking. Optical images showing the fabrication of a typical hBN/graphene/hBN stack using the PMMA stamp method in UHV are shown in **Fig. S8**. It is of note that in the AFM image shown in **Fig. S8d**, a small amounts of hydrocarbon contamination, in the form of bubbles, can be observed around the edge of the encapsulated graphene although, clean regions on the order 10 μm x 10 μm are still readily achievable.

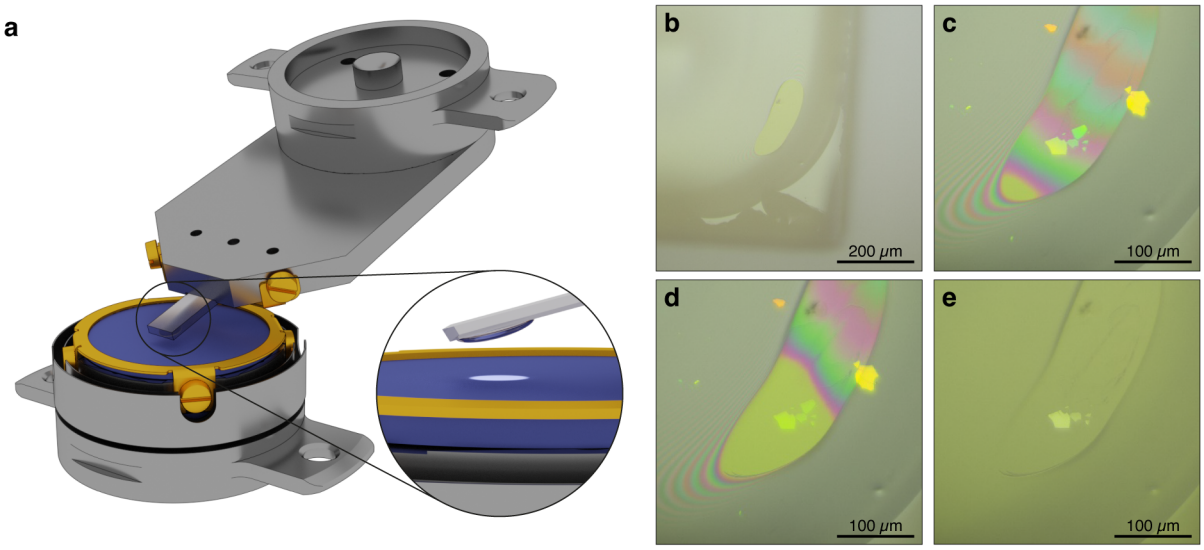

Figure S7. Optical image sequence demonstrating the formation of a melt spot and subsequent flakes pickup in UHV using the polymer stamp method. *(a) Glass slide with a droplet of PMMA on the end is brought into contact with a target substrate below an optical objective. (b) A spot on the PMMA meniscus is melted to create a flattened region. (c,d) Target hBN crystal is selected and the flattened region of PMMA is brought into contact. (e) PMMA is rapidly retracted resulting in a successful pickup.*

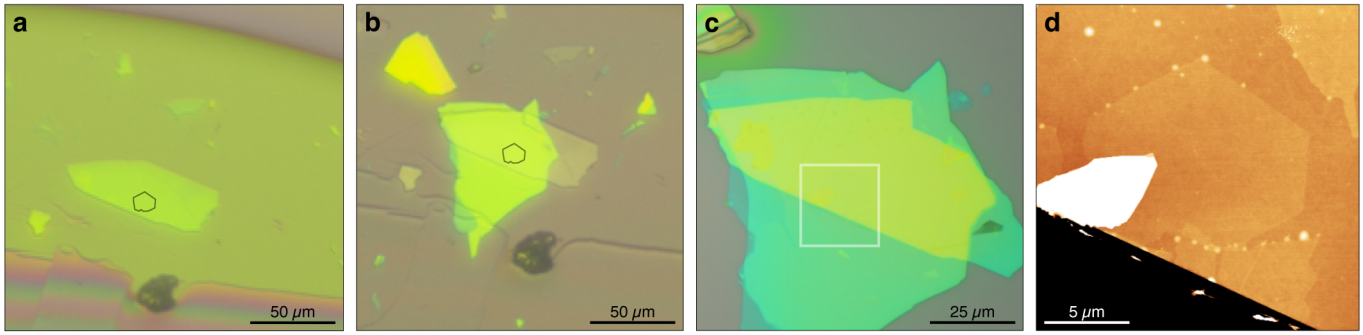

Figure S8. Sequence to fabricate hBN/graphene/hBN heterostructures in UHV using the polymer stamp method. *(a) hBN is picked up with the PMMA and deposited onto a target graphene sample (black dashed outline). (b) hBN/Graphene stack is aligned above a substrate hBN crystal. (c) hBN/Graphene is stamped onto the substrate hBN creating the hBN/Graphene/hBN heterostructure. (d) AFM of fully encapsulated graphene for the region indicated by the white dashed square in (c). Small pockets of contamination (white spots) can be observed around the edges of the graphene.*

7 Atomic Force Microscopy

AFM topography and conductive AFM (c-AFM) maps were acquired on twisted graphene (TG) samples deposited on top of hBN flakes using a Cypher-S AFM (*Asylum Research*) in a cleanroom environment. To allow access to the exposed twisted bilayer graphene, the cantilever has been deposited on a SiO_2 wafer facing upwards. To ensure a reliable electrical contact during the c-AFM measurements a stencil mask was employed to deposit a 150 nm Au film contacting the TG region.

All cAFM measurements were performed with Multi75E-G Cr-Pt coated tips from *Budget Sensors.* The topography scans were acquired over large areas $(\sim\mu m^2)$ in tapping mode in order to minimise any possible damage to the samples. C-AFM scans were performed in several different regions of the samples, allowing us to observe and study the moiré pattern uniformity. In all cases, the measurements were acquired in contact mode over $50\ nm\ \times 50\ nm$ areas, with a constant tip-sample potential difference of $-50\ mV,$ and at relatively high scan rate: $1.50 - 1.75\ Hz$ to avoid contribution of the thermal drift.

Values of the twist angle, θ_{twist}, were calculated from the c-AFM scans using an in-house developed Python code. For each of the c-AFM maps recorded, we started by applying a line by line median filter along the direction of the slow scan axis, i.e. y-axis in our case, in order to remove low-frequency noise. Following this, we extracted periodograms for each of the lines along the fast scan axis, and then summed them to generate a magnitude spectrum in the scanning direction. By plotting the periodogram with respect to the inverse frequencies, we observed some peaks corresponding to the moiré periodicity, which we then fitted with Gaussian profiles to obtain information on the magnitude of the moiré wavelength in the x-direction, λ_x. By performing the analysis following the described method, we reduce the effect of the temporal drift which is more noticeable in the slow scan axis and can distort the observed moiré pattern, and thus the measured twist angle.

In the cases in which the high-symmetry direction of the moiré lattice was not aligned with the fast-scan axis, we calculated the angle withstood by both directions, α, and then applied a trigonometric transformation to obtain the period of the moiré lattice $\lambda = \lambda_x/\cos\alpha$. Finally, the moire angle was calculated using the following the relationship:

$$\theta_{twist} = \cos^{-1}\left(1 - \frac{a^2}{2\lambda^2}\right)$$

where a is the lattice constant of graphene.

8 Cross-sectional STEM and EDX

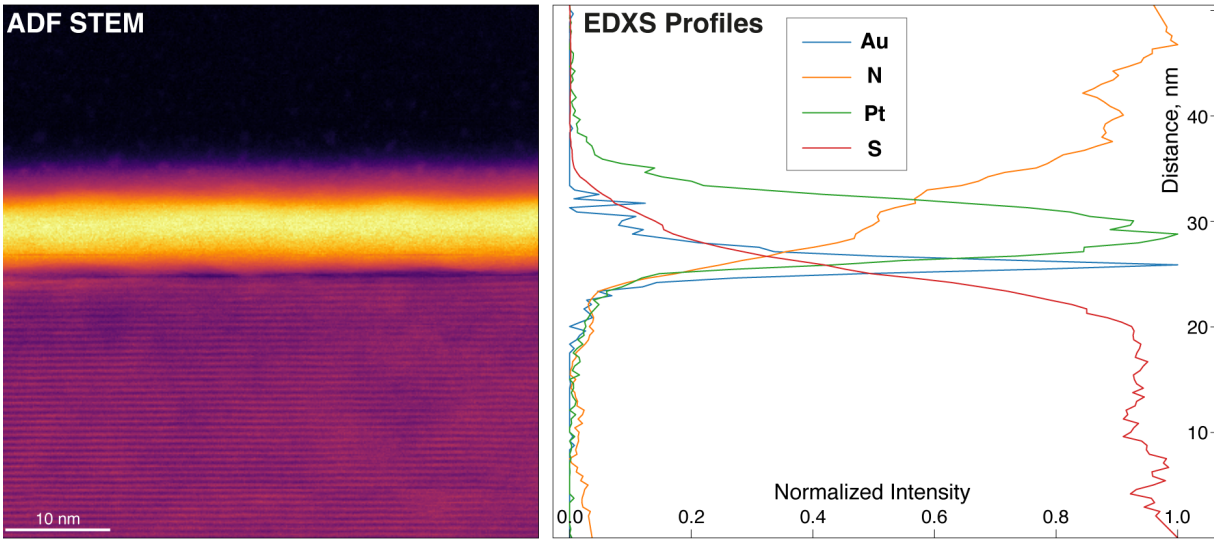

Figure S9. Cross-sectional scanning transmission electron microscopy (STEM) energy dispersive X-ray spectroscopy (EDX) characterization. *(a) Annular dark field (ADF) STEM image of cross section of a cantilever with an adhered thick MoS_2 flake prepared with a conventional focused ion beam (FIB) lift-out approach. Data acquired on a probe corrected FEI Titan G2 80-200 S/TEM operating at a 200 kV accelerating voltage. The STEM data was acquired with a probe current of 180 pA, a semi-convergence angle of 21.5 mrad and ADF inner angle of 43 mrad. (b) STEM EDX elemental mapping showing normalized intensity profiles for the x-ray lines (Au Lα, Pt Kα, S Kα and N Kα). The spectral image was summed parallel to the interface to produce the intensity line scans corresponding to the image in (a). EDX STEM elemental mapping was acquired with a quad detector ChemiSTEM EDX system, a pixel dwell time of 40 µs and a total acquisition time of 660 seconds.*

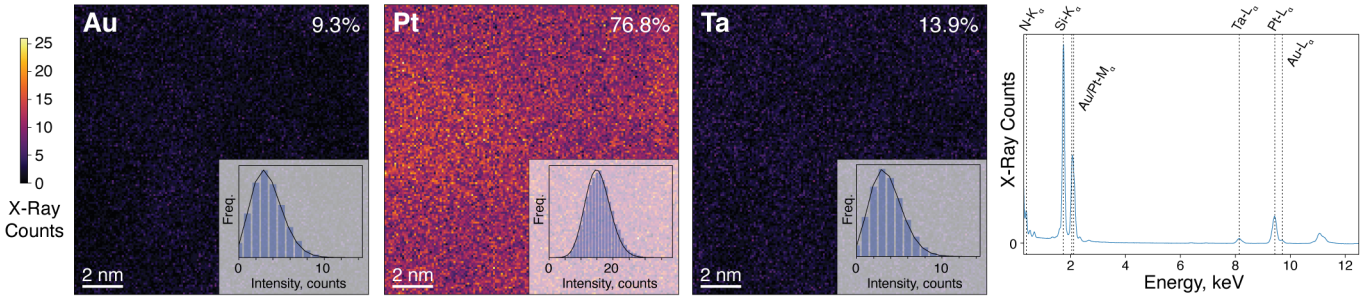

Figure S10. Plan view scanning transmission electron microscopy (STEM) energy dispersive X-ray spectroscopy (EDX) characterization of metals deposited on the cantilever surface. *(**a,b,c**) STEM EDX elemental mapping showing intensity distribution for the x-ray lines Au Lα (a), Pt Lα (b), Ta Lα (c). Insets show signal histograms integrated over the image area, fit to a Poisson distribution, indicating a signal distribution consistent with a constant metal concentration measured in a low-count regime.(d) EDX spectrum with the characteristic X-ray lines highlighted.*

9 Mobilities Comparison

Table S2. Mobilities comparison (Drude Model). *Polymer-assisted fabrication of hBN encapsulated monolayer graphene devices and mobilities calculated from the Drude model of conductivity, $\sigma = \mu ne$, where μ is the charge carrier mobility.*

No.	$\mu \times 10^6$ ($cm^2V^{-1}s^{-1}$)	$n \times 10^{12}$ (cm^{-2})	T(K)	Reference name	DOI	Year
1	0.100	0.1	4	Micrometre-Scale Ballistic Transport in Encapsulated Graphene at Room Temperature	10.1021/nl200758b	2011
2	0.080	0.1	10	Cloning of Dirac fermions in graphene superlattices	10.1038/nature12187	2013
3	0.500	<2	3	Electronic Properties of Graphene Encapsulated with Different Two-Dimensional Atomic Crystals	10.1021/nl5006542	2014
4	0.120	0.1	2	Selective Equilibration of Spin-Polarized Quantum Hall Edge States in Graphene	10.1103/ PhysRevLett.112.196601	2014
5	0.120		2	Hierarchy of Hofstadter states and replica quantum Hall ferromagnetism in graphene superlattices	10.1038/nphys2979	2014
6	0.35	0.5	1.6	Ultrahigh-mobility graphene devices from chemical vapor deposition on reusable copper	10.1126/sciadv.1500222	2015
7	0.300	0.1	20	Quantum oscillations of the critical current and high-field superconducting proximity in ballistic graphene	10.1038/nphys3592	2015
8	0.150		16	Size quantization of Dirac fermions in graphene constrictions	10.1038/ncomms11528	2016
9	0.117	0.5	300	The hot pick-up technique for batch assembly of van der Waals heterostructures	10.1038/ncomms11894	2016
10	0.200	1	0.05	Tunable transmission of quantum Hall edge channels with full degeneracy lifting in split-gated graphene devices	10.1038/ncomms14983	2017
11	0.207	0.8	70	High Velocity Saturation in Graphene Encapsulated by Hexagonal Boron Nitrid	10.1021/ acsnano.7b03878	2017
12	0.250	Near DP	1.5	Observation of the quantum valley Hall state in ballistic graphene superlattices	10.1126/sciadv.aaq0194	2018
13	0.120	0.1	9	High-Mobility, Wet-Transferred Graphene Grown by Chemical Vapor Deposition	10.1021/ acsnano.9b02621	2019

No.	μ x10^6 (cm^{2}V^{-1}s^{-1})	n x10^{12} (cm^{-2})	T (K)	Reference name	Link	Year
14	0.011	1.5	4	Electron transport and the effect of current annealing in a two-point contacted hBN/graphene/hBN heterostructure device	10.1063/5.0016471	2020
15	0.220	0.05	9	Topological valley currents via ballistic edge modes in graphene superlattices near the primary Dirac point	10.1038/ s42005-020-00495-y	2020
16	0.200	0.1	6	Localization to delocalization probed by magnetotransport of hBN/graphene/hBN stacks in the ultra-clean regime	10.1038/ s41598-021-98266-4	2021
17	0.130	1.5	20	Tunable Spin Injection in High-Quality Graphene with One-Dimensional Contacts	10.1021/ acs.nanolett.1c03625	2022
18	1.000	2	1.5	Mechanisms of Interface Cleaning in Heterostructures Made from Polymer-Contaminated Graphene	10.1002/smll.202201248	2022
19	1.300	2	5	The University of Manchester	10.1038/ s41467-020-15829-1	2016-2022
20	0.800	1	5	The University of Manchester	n/a	2016-2022
21	0.600	1	5		n/a	
22	2.000	1	0.01		10.1038/ s41467-020-19604-0	
23	0.100	0.1	2		n/a	
24	0.300	0.1	2		n/a	
25	0.100	0.1	2		n/a	
26	0.150	1	4		n/a	
27	0.750	-3.3	5		n/a	
28	0.500	0.2	10		n/a	

Table S3. Mobilities comparison (MFP). *Polymer-assisted and our SiN_x cantilever fabrication of hBN encapsulated monolayer graphene devices and mobilities calculated from mean free path.*

No.	Mobility x10^6 ($cm^2V^{-1}s^{-1}$)	nx10^{12} (cm^{-2})	T(K)	Reference name	DOI	Year
1	1	3	1.7	One-Dimensional Electrical Contact to a Two-Dimensional Material	10.1126/ science.1244358	2013
2	3	0.6	1.8	Ballistic Transport Exceeding 28 μm in CVD Grown Graphene	10.1021/ acs.nanolett. 5b04840	2016
3	1.8	-1.5 → 0	9	Cleaning interfaces in layered materials heterostructures	10.1038/ s41467-018-07558-3	2018
4	0.75 (W=5.0 um)	-0.5	5	Our devices		
4	1.2 (W=12.5um)	-0.5	5			
5	3.5 (W=33.6um)	-1	4			
6	2.0 (W=23um)	-0.5	1.5			